IEEE Access
Multidisciplinary | Rapid Review | Open Access Journal

Received June 5, 2019, accepted July 1, 2019, date of publication July 5, 2019, date of current version July 30, 2019.

Digital Object Identifier 10.1109/ACCESS.2019.2927010

An Actuator Fault Detection and Reconstruction Scheme for Hex-Rotor Unmanned Aerial Vehicle

RIJUN WANG[1], CHANGJUN ZHAO[2], YUE BAI[3], WENHUA DU[1], AND JUNYUAN WANG[1]

[1]School of Mechanical Engineering, North University of China, Taiyuan 030051, China
[2]China Electronic Product Reliability and Environmental Testing Research Institute, Guangzhou 510000, China
[3]Changchun Institute of Optics, Fine Mechanics and Physics, Chinese Academy of Sciences, Changchun 130033, China

Corresponding authors: Rijun Wang (wangrijun1982@ 126.com), Changjun Zhao (zhaocj916@163.com), and Yue Bai (baiy@ciomp.ac.cn)

This work was supported in part by the National Natural Science Foundation of China under Grant 161304017, and in part by the Natural Science Foundation of Shanxi Province of China under Grant 201801D121187 and Grant 201801D221237.

ABSTRACT The detection and the reconstruction of actuator faults in a flight control system are crucial to avoid negative impacts on the aircraft itself, as well as human and environmental systems. In this paper, an actuator fault detection and reconstruction scheme based on fault classification for the hex-rotor unmanned aerial vehicle are designed. First, the fault type of actuator is analyzed and classified, then an actuator fault model is established based on multiple fault classification. Second, a fault detection and reconstruction (FDR) scheme for the hex-rotor unmanned aerial vehicle is proposed. In the proposed scheme, a fault observer group based on an extended Kalman filter (EKF) is designed for fault detection and isolation, and the flight state feedback required by the fault observer group is provided by the multi-sensor navigation unit (MSNU). Then, a fault reconstruction algorithm of the actuator is proposed by using the output of the fault observer group. The designed FDR system is applied to hex-rotor unmanned aerial vehicle prototype for its evaluation. The simulation results show that the proposed design is capable of fault detection and the reconstruction of actuator faults, and the actual flight verifies the effectiveness of the proposed methods.

INDEX TERMS Unmanned aerial vehicle, actuator fault, multi-sensor navigation unit, fault observer, EKF, reconfigurable controller.

I. INTRODUCTION

Multi-rotor unmanned aerial vehicles (mUAV) have been extensive applied in military and civilian fields, including for security patrols, search and rescue in hazardous environment, surveillance and classification, attack, and rendezvous [1], [2]. Consequently, the aircraft safety accidents caused by actuator faults have also increased dramatically all over the world, having negative impacts on human and environmental systems. Therefore, research into fault-tolerant control (FTC) technology for mUAV has become critical for improving the safety and reliability of mUAV [3]–[6].

FTC technology, widely used in many fields of astronautics and aerospace [7]–[16], can remove the influence of faults independently, and maintain the quality of the system. Generally, the FTC system of mUAV includes fault detection (FD) and control reconfiguration. FD is an important component in the construction of FTC systems for mUAV. FD in control problems of mUAV has received a great deal of attention in recent years [17], [18]. Due to the fact that fault occurrence in aeronautical systems can lead to irreparable financial loss and injuries, early detection of faults plays an important role in a flight control system. In the case of fault occurrence in an actuator, the flying performance of mUAV may degrade, which may cause partial loss of the control action of the actuator. Thus, in order to have a safe flight controller, it is essential to compensate for the faults that occurred. Conventional approaches to fault detection in actuators are mainly based on hardware redundancy techniques. However, due to the limitations of size, weight, and cost in the design of mUAVs, hardware redundancy is not a feasible solution for the design of fault-tolerant systems for mUAVs. Therefore, the idea of analytical redundancy has been proposed as an alternative solution [19]–[23]. The majority of FD techniques in UAVs are based on observer and parameter estimation technology [24]–[26]. Some exciting results have been obtained using a sliding mode observer [27]–[29], a two-stage Kalman filter [30], an adaptive Thau observer [31], and sliding mode techniques [32]. The passive fault tolerant control (PFTC) is proposed in [33], [34], which requires the fault estimation.

The associate editor coordinating the review of this manuscript and approving it for publication was Maurizio Magarini.

But this proposed approach becomes very difficult when a severe fault occurs. In order to deal with several classes of fault, the FTC based on the combination between backstepping control and adaptive interval type-2 fuzzy inference systems is given in [35], and applied to the hexarotor and quadrotor helicopters.

In this paper, according to the fault detection and reconstruction problem of the actuator, a lift model of actuator is built on the basis of fault occurrence. The actuator faults are divided into two categories, i.e. failure and gain fault. To perform quick and accurate detection of the fault of each actuator, and to determine the location and type of the fault, a set of fault observers (FOB) based on EKF is designed, combined with the state feedback of the mUAV provided by the multi-sensor navigation unit (MSNU). In addition, a self-reconfiguration algorithm based on fault classification is designed, which can be used to reconstruct the different actuator faults according to the output signal of the FOB, so as to ensure the safety and reliability of the flight. Based on the theoretical analysis, the related research is verified by numerical simulation and actual flight. In comparison with actuator fault detection and reconstruction design for mUAV in the existing literature, the main contributions of this research work are twofold. First, on the premise of in-depth analysis of the frequently occurring actuator fault types, a novel actuator lift model based on fault classification is developed. Secondly, a fault detection and reconstruction strategy based on actuator fault classification for the Hex-rotor UAV is proposed.

The paper is organized as follows: Section 2 describes the fault model of actuator based on fault classification. Our proposed fault detection and reconstruction strategy is illustrated and the FDR design for the Hex-rotor UAV is presented in Section 3. The numerical simulation and experimental results are illustrated in Section 4. The conclusions are provided in Section 5.

II. PROBLEM FORMULATION

A. INTRODUCTION OF HEX-ROTOR UAV

As a kind of mUAV, the Hex-rotor UAV can improve the structure of conventional planar mUAV without significantly increasing the weight of the aircraft [36]. It can effectively improve the carrying capacity and flight endurance, and enhance the control moment of the yaw channel. The three-dimensional structure diagram and structural principle of Hex-rotor UAV are shown in FIGURE 1(a) and FIGURE 1(b), respectively.

From the figures we know that the Hex-rotor UAV has symmetry. The six carbon fiber connecting rods are of equal length located on the same plane, and distributed around the center of the aircraft evenly. The six actuators are vertically installed at the end of the connecting rod, each of which consists of a motor and a rotor.

The physical parameters of the prototype are shown in TABLE 1.

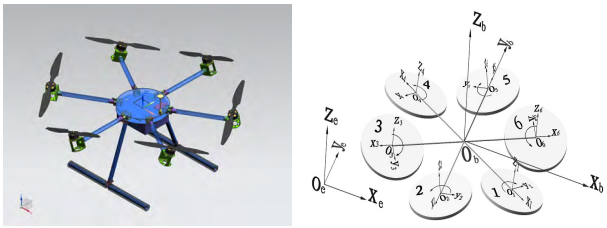

FIGURE 1. Hex-rotor UAV. (a) 3D structure. (b) Structural schematic.

TABLE 1. Physical parameters of the prototype.

Physical parameters	Value
Maximum take-off weight	7.5kg
Empty weight	3.95kg
Distance between the actuator and the center	0.45m
Lift factor (at atmospheric pressure)	1.91×10^{-3}
Torsional moment factor (at atmospheric pressure)	4.21×10^{-5}
Moment of inertia I_x	0.363 kg•m^2
Moment of inertia I_y	0.363 kg•m^2
Moment of inertia I_z	0.651 kg•m^2

The O_b is the origin of body coordinate system $O_bx_by_bz_b$, which is located on the center of mass of the aircraft. The inertial coordinate system $O_ex_ey_ez_e$ selects the "north, west, and up" coordinate system, and the origin O_e coincides with O_b. The rotary shaft of each executive unit and the O_bz_b axis of the body coordinate system become angle γ ($\gamma = 10°$). The two adjacent motor axes point to the opposite direction. The two centrally symmetric rotors are in the same plane, such as rotors 1 and 4, rotors 2 and 5, and rotors 3 and 6. Depending on this novel layout structure, the aircraft can achieve arbitrary configuration of 6-DOF motion (within the range of the rotor's driving capacity) by adjusting the rotational speeds of the six actuators.

B. FAULT TYPE OF ACTUATOR

For the Hex-rotor UAV, more than 95% of the power is consumed by the actuators. Compared to other units of Hex-Rotor UAV, due to the heavy workload, high temperature, mechanical vibration, and aging components, the actuator is more prone to failure. In addition, the number of actuators in the Hex-rotor UAV increases the probability of failure. Once the actuator has a failure, it often causes the aircraft to lose control or even crash. Therefore, it is necessary to improve the reliability of the actuator.

In this paper, the mentioned Hex-rotor UAV has six actuators. Each of them is composed of a three-phase brushless DC motor (BLDCM), a rotor, and a driving circuit board (as shown in FIGURE 2). This section will analyze the lift fault model of the actuator in considering the conditions of the motor fault, the drive circuit board failure, and the rotor fault. It provides a theoretical basis for the design of the FDR system.

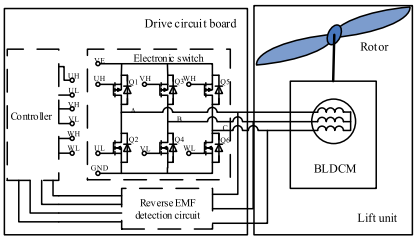

FIGURE 2. Block diagram of the actuator.

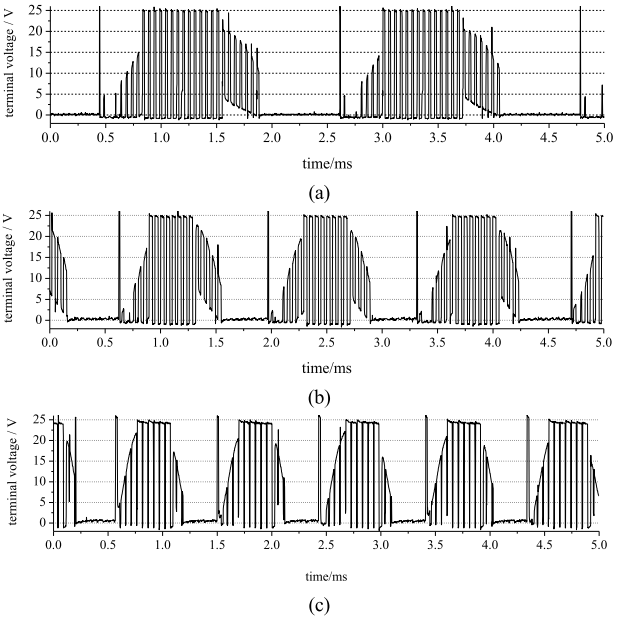

FIGURE 3. Different terminal duty voltage waveforms under normal operation. (a) The duty cycle is 30%. (b) The duty cycle is 60%. (c) The duty cycle is 90%.

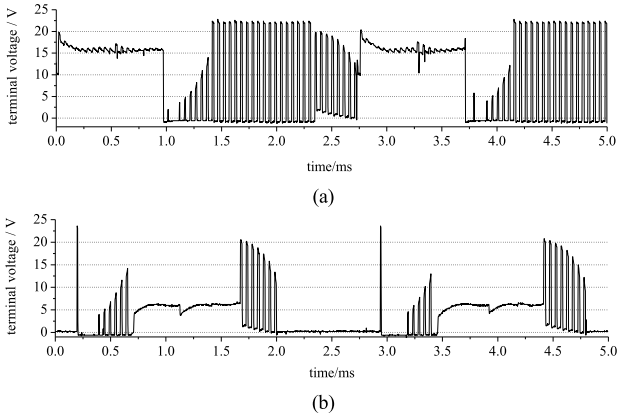

FIGURE 4. Terminal voltage waveform under MOSFET fault. (a) Short circuit of lower bridge. (b) Short circuit of upper bridge.

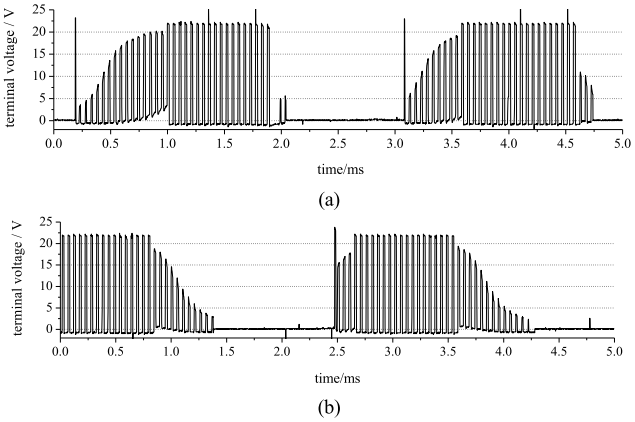

FIGURE 5. Terminal voltage waveform under the phase-changing failure. (a) Lag phase-changing. (b) Forward phase-changing.

1) THE DRIVE CIRCUIT BOARD FAULT

During the flight, the drive circuit board in the actuator has high load, high temperature, and fast aging of electronic components, which makes the failure rate of the drive circuit board high, and seriously threatens the safe flight of the aircraft. The main faults of the drive circuit board include open circuit fault, phase-changing fault, short circuit fault, etc.

a: OPEN CIRCUIT OF THREE-PHASE FULL CONTROL BRIDGE

The actuator adopts a three-phase full control bridge circuit to drive BLDCM. The full control bridge circuit is composed of power MOSFET and its driving circuit. In the absence of a fault, the output waveform of the terminal voltage is controlled by the modulated signal of fully control bridge. Taking the terminal voltage of phase A as an example, the output waveform diagram is shown in FIGURE 3. It can be seen that the terminal voltage is not only consistent with the modulated signal, but also the time interval between the six sectors in an electric cycle is uniform. In addition, with the increase of duty cycle, the electric cycle decreases and the speed of BLDCM increases.

The terminal voltage waveform will no longer be consistent with the modulated signal when an open circuit occurs. In FIGURE 4, it is shown that the terminal voltage of the fault phase will be greatly distorted. Meanwhile, the speed will decrease. However, the time interval between the six sectors in an electric cycle will not be affected. In addition, after the occurrence of an open circuit of the full control bridge circuit, the drive circuit board cannot ensure that the reactive magnetic field produced by the circuit is perpendicular to the stator magnetic field, causing the output torque of the motor to be reduced. At this point, the BLDCM will be in a low efficiency running state and has excessive heat, which may develop into more serious faults such as the MOSFET breakdown short circuit fault, etc.

b: PHASE-CHANGING FAILURE

When phase-changing failure occurs, the driving circuit board cannot get the accurate signal of phase-changing, which leads to phase-changing failure. There are two cases of phase-changing, namely, the lag phase-changing and the forward phase-changing. As shown in FIGURE 5, the failure of both ways will make the time interval of the six sectors uneven.

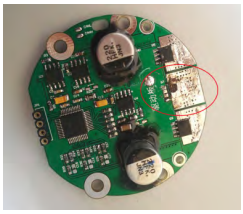

FIGURE 6. MOSFET breakdown.

FIGURE 7. Short circuit fault of the actuator.

Phase-changing failure usually has a variety of reasons, such as switch noise of three-phase full control bridge circuit, the continuous current process of inductance of windings, etc. These reasons can cause the controllers to misjudge the phase-changing signal. Therefore, it is necessary to add the judgment process into the phase-changing algorithm of the controller. In the same way, the phase-changing failure also makes the efficiency of the motor lower.

c: MOSFET BREAKDOWN

Subject to the MOSFET package and the small position of assembly, in this case, the MOSFET temperature will rise rapidly, causing MOSFET to leave the safe operating area (SOA). Eventually, as shown in FIGURE 6, the MOSFET will enter the short-circuit state due to over-current breakdown. Under the condition of limited battery output power, this state may lead to a very serious drop in the bus voltage, so that the aircraft is completely out of control.

2) BLDCM FAULT

The BLDCM fault may cause a decrease or even disappearance of the induced electromotive force (EMF). According to the voltage balance equation of the BLDCM, as the induced EMF decreases, the armature current will inevitably increase. In this case, the heating of the BLDCM is serious and the operational efficiency is reduced, which further deteriorates the situation, and even causes the induced EMF to be close to zero.

When the induced EMF is reduced to zero, the supply voltage is applied directly to the equivalent resistance of the coil windings. As the equivalent resistance of the coil windings is very small, typically a few hundred milliohms, a tremendous amount of armature current is generated. The large armature current is most likely to cause breakdown of the MOSFET, resulting in the BLDCM burnout (as shown in FIGURE 7), which seriously compromises the system.

In summary, the drive board fault and motor failure will make the actuator be in low efficiency operation, which will cause a serious breakdown if a short-circuit fault occurs. Therefore, for the entire flight system, the safest approach is to stop the corresponding actuator when a drive board fault or motor fault is detected, and upload the fault information to the operational layer to activate the self-reconfigurable controller.

3) ROTOR FAULT

In addition to the above two faults, the other type of fault is rotor failure. The rotor is an important element that provides lift for the Hex-Rotor UAV, but the rotor often appears to be loosening due to rotor damage, surface damage, severe wear at joints, etc., which leads to the possibility of rotor fault. Usually, on assuming that the rotor speed is constant, the rotor can provide a constant lift for the Hex-Rotor UAV. Once the rotor failure occurs, the aerodynamic characteristics of the aircraft are changed, and the lift force provided to the aircraft fluctuates. The lift force provided by the rotor is significantly reduced or even lost, which seriously affects the stability and safety of the Hex-Rotor UAV.

Based on the above analysis, the common faults of the actuator are summarized as follows.

TABLE 2. Common faults of actuator.

Fault location	Fault type
The drive circuit board fault	short circuit of lower bridge, short circuit of upper bridge, open circuit of lower bridge, open circuit of upper bridge, lag phase-changing, forward phase-changing, failure of CAN bus communication, low battery, malfunction of other components, etc.
BLDCM fault	interphase short circuit, a phase winding open circuit, magnetic steel separation, etc.
Rotor fault	rotor loosening, rotor damage, wing damage, connector wear, etc.

C. MODELING OF ACTUATOR BASED ON FAULT CLASSIFICATION

In this section, the impact of the fault on the actuator model is discussed. The faults are summarized in TABLE 2. Based on the discussion, the model of the actuator under the condition of fault is obtained.

Generally, the lift model provided by the actuator can be described as [37]:

$$f = k\Omega^2 \tag{1}$$

where f is the lift force provided by the actuator, k is the factor of lift force, and varies with environmental parameters. Ω is the rotor speed. As can be seen in Equation (1), the performance of the fault of the actuator is the change of the lift force (in other words, the change of the lift factor or the rotor speed). Naturally, the fault of the actuator can be divided into two cases, that is Ω cannot reach the desired speed or k less than the normal value. In order to facilitate analysis, gain fault and failure are introduced to describe the cases.

The gain fault of the actuator is when lift factor k is smaller than the normal range. If the actuator can only provide partial lift force at the same speed, then the gain fault can be described as:

$$f_i(t) = (1 - \beta_i)\,\bar{k}_i \Omega_i^2 \tag{2}$$

where $\bar{k}_i$ is the lift factor measured in the indoor standard atmospheric pressure, and $i = 1, 2, 3 \ldots, 6$. Ω_i is the speed of the i-th rotor, and $f_i(t)$ indicates the actual lift force produced by the i-th actuator. β_i is called the damage proportionality coefficient, and $0 < \beta_i < 1$. It can be seen that the larger β_i is, the smaller the actual output of lift force of the rotor.

When rotor fault occurs, the lift factor is significantly smaller than the normal value. Although the motor and rotor can continue to work, the actuator can only provide partial lift. It can be seen that the rotor fault belongs to the gain fault of the actuator.

The failure of the actuator means that the actuator does not have the ability to provide lift force for the Hex-Rotor UAV in the working state. Then the failure can be described as:

$$f_i(t) = 0 \tag{3}$$

When the BLDCM fault occurs in the actuator, its speed cannot reach the desired speed or even zero. If it is not handled in time, there is a risk of drive circuit board fault. Therefore, when the BLDCM fault is detected, the fault motor will stop working and the BLDCM fault can be attributed to the failure of the actuator.

The drive circuit board fault is similar to the BLDCM fault, and its speed cannot reach the desired speed or even zero. The driving circuit board fault is a type of electrical fault; it is very likely to deteriorate in a short time, and the serious danger is hidden. In order to avoid risks, the actuator of the fault will stop working. The driver circuit board failure is also attributed to the failure.

Based on the above discussion, the common faults of the actuator of Hex-Rotor UAV can be classified into two categories, namely gain fault and failure. The actuator model based on fault classification can be described as:

$$f_i(t) = (1 - \beta_i)\,\bar{k}_i \Omega_i^2 \quad i = 1, 2 \cdots 6 \tag{4}$$

III. FAULT DETECTION AND RECONSTRUCTION (FDR) SYSTEM DESIGN

According to the fault classification of the actuator, a FDR system is designed as shown in FIGURE 8. It can be seen that the state transition matrix of the FOB and the control input matrix are obtained through the dynamic model of the aircraft, and the measurement matrix is obtained by the MSNU; then the lift factor of the rotor is estimated online. The FOB based on EKF estimates the lift factor of the corresponding actuator online by the estimated lift factor of the corresponding actuator and realizes the detection of failure and gain faults. When the actuator failure occurs, the corresponding self-reconfiguration algorithm for different faults can effectively guarantee the safety of the aircraft system.

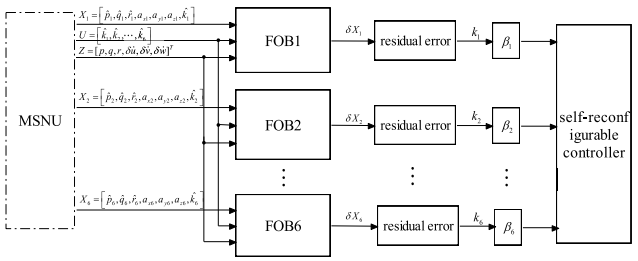

FIGURE 8. Architecture of FDR system.

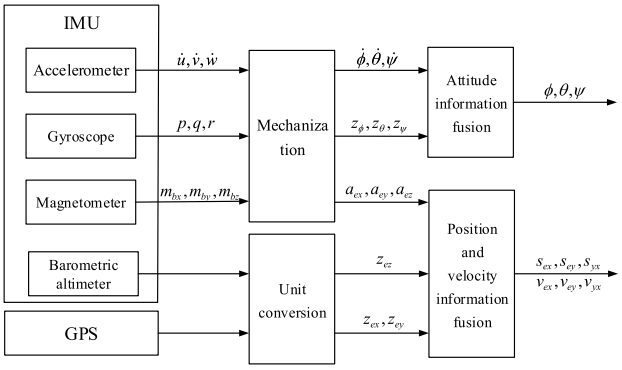

FIGURE 9. Multi-sensor navigation unit flow chart.

A. MULTI-SENSOR NAVIGATION UNIT

The FOB group needs the feedback of flight state by the fusion of MSNU, which consists of the microprocessor (STM32F103), the inertial measurement unit (IMU) (ADIS16448), and the GPS module (LEA- 6H). The IMU includes a three-axes gyroscope, a three-axes accelerometer, a three-axes magnetometer, a pressure gauge, and a thermometer. The measurement data of each type of sensor have their own characteristics. For example, the Micro-Electro-Mechanical System (MEMS) gyroscope has higher angular accuracy in the short term, but large cumulative errors and serious integration drift. At a constant speed of aircraft, using the accelerometer to solve the attitude angle does not cause the cumulative error problem, but the data accuracy is poorer. In this case, the data of the two sensors are fused by a Kalman filter (KF) to increase the estimation accuracy of the attitude angle. The data fusion flow of MSNU is shown in FIGURE 9.

As shown in FIGURE 9, if the IMU obtains the data of the three-axes gyroscope, three-axes accelerometer, and three-axes magnetometer, then $\dot{\phi}$, $\dot{\theta}$, $\dot{\psi}$ and z_ϕ, z_θ, z_ψ are obtained by the mechanical arrangement [37]. Next, the aircraft attitude angular data fusion process can be treated as a linear equation, and the state equation and measurement equation are obtained as follows:

$$\boldsymbol{X}_{\eta.k} = \boldsymbol{\Phi}_{\eta.k,k-1}\boldsymbol{X}_{\eta.k-1} + \boldsymbol{\Gamma}_{\eta.k,k-1}\dot{\boldsymbol{X}}_{\eta.k} + \boldsymbol{\Gamma}_{\eta.k,k-1}\boldsymbol{Q}_\eta \tag{5}$$

$$\boldsymbol{Z}_{\eta.k} = \boldsymbol{H}_{\eta.k}\boldsymbol{X}_{\eta.k} + \boldsymbol{R}_{\eta.k} \tag{6}$$

where $\boldsymbol{X}_{\eta,k} = [\phi, \theta, \psi]^T$ is the attitude angular vector, $\boldsymbol{\Phi}_{\eta.k,k-1} = diag\,(1, 1, 1)$, $\boldsymbol{\Gamma}_{\eta.k,k-1} = diag\,(T_s, T_s, T_s)$, $\boldsymbol{H}_{\eta.k} = diag\,(1, 1, 1)$, $\boldsymbol{Z}_{\eta.k} = [z_{\phi.k}, z_{\theta.k}, z_{\psi.k}]^{\mathrm{T}}$ is the observation sequence, the three-dimensional system process noise

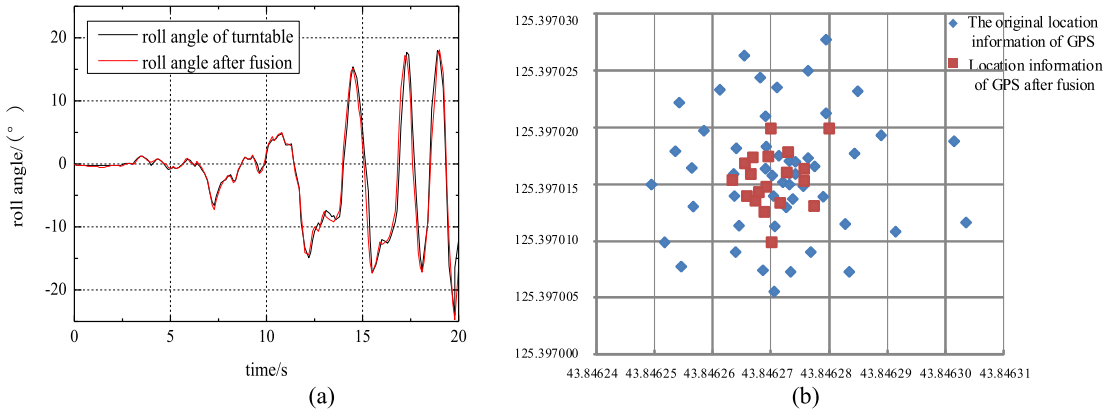

FIGURE 10. MSNU data fusion results. (a) Roll angle fusion. (b) GPS location information fusion.

sequence is $\boldsymbol{Q}_\eta = [w_\phi, w_\theta, w_\psi]^{\mathrm{T}}$, in which w_ϕ, w_θ, w_ψ is determined by the gyroscope's own performance and subsequent processing, and the three-dimensional noise sequence $\boldsymbol{R}_{\eta.k} = [v_{\phi.k}, v_{\theta.k}, v_{\psi.k}]^{\mathrm{T}}$.

In the same way, relative to the space position and the line velocity, the equation of state and the measurement equation of the KF are as follows:

$$\boldsymbol{X}_{e.k} = \boldsymbol{\Phi}_{e.k,k-1}\boldsymbol{X}_{e.k-1} + \boldsymbol{\Gamma}_{e.k,k-1}\boldsymbol{a}_{e.k} + \boldsymbol{\Gamma}_{e.k,k-1}\boldsymbol{Q}_e \quad (7)$$

$$\boldsymbol{Z}_{e.k} = \boldsymbol{H}_{e.k}\boldsymbol{X}_{e.k} + \boldsymbol{R}_{e.k} \quad (8)$$

where, $\boldsymbol{X}_{e.k} = [s_{ex.k}, v_{ex.k}, s_{ey.k}, v_{ey.k}, s_{ez.k}, v_{ez.k}]^{\mathrm{T}}$ is the position and velocity information of the inertial coordinate system, $\boldsymbol{a}_{e.k} = [a_{ex.k}, a_{ey.k}, a_{ez.k}]^{\mathrm{T}}$ is the acceleration information in the inertial coordinate system, $\boldsymbol{Q}_e = [w_{sx.k}, w_{vx.k}, w_{sy.k}, w_{vy.k}, w_{sz.k}, w_{vz.k}]^{\mathrm{T}}$ is the system process noise sequence, $\boldsymbol{R}_{e.k} = [v_{sx.k}, v_{sy.k}, v_{sz.k}]^{\mathrm{T}}$ is the noise sequence, and $\boldsymbol{Z}_{e.k} = [z_{ex.k}, z_{ey.k}, z_{ez.k}]^{\mathrm{T}}$ is the observation vector.

In this paper, the process noise is regarded as a fixed constant, and the observation noise is estimated by the Sage-Husa adaptive algorithm [38] in real time. The steps are as follows:

$$\begin{cases} \hat{\boldsymbol{X}}_{k/k-1} = \boldsymbol{\Phi}_{k/k-1}\hat{\boldsymbol{X}}_{k-1} + \boldsymbol{\Gamma}_{k,k-1}\dot{\boldsymbol{X}}_{k-1} \\ \hat{\boldsymbol{X}}_k = \hat{\boldsymbol{X}}_{k/k-1} + \boldsymbol{K}_k\boldsymbol{v}_k \\ \boldsymbol{v}_k = \boldsymbol{Z}_k - \boldsymbol{H}_k\hat{\boldsymbol{X}}_{k/k-1} \\ \boldsymbol{K}_k = \boldsymbol{P}_k\boldsymbol{H}_k^T\left[\boldsymbol{H}_k\boldsymbol{P}_{k/k-1}\boldsymbol{H}_k^{\mathrm{T}} + \hat{\boldsymbol{R}}_k\right]^{-1} \\ \boldsymbol{P}_{k/k-1} = \boldsymbol{\Phi}_{k/k-1}\boldsymbol{P}_{k-1}\boldsymbol{\Phi}_{k/k-1}^{\mathrm{T}} + \boldsymbol{\Gamma}_{k,k-1}\boldsymbol{Q}_{k-1}\boldsymbol{\Gamma}_{k,k-1}^{\mathrm{T}} \\ \boldsymbol{P}_k = (\boldsymbol{I} - \boldsymbol{K}_k\boldsymbol{H}_k)\boldsymbol{P}_{k/k-1}(\boldsymbol{I} - \boldsymbol{K}_k\boldsymbol{H}_k)^{\mathrm{T}} + \boldsymbol{K}_k\hat{\boldsymbol{R}}_k\boldsymbol{K}_k^{\mathrm{T}} \\ \hat{\boldsymbol{R}}_k = (1 - d_k)\hat{\boldsymbol{R}}_{k-1} \\ \quad + d_k\left[(\boldsymbol{I} - \boldsymbol{H}_k\boldsymbol{K}_{k-1})\boldsymbol{v}_k\boldsymbol{v}_k^{\mathrm{T}}(\boldsymbol{I} - \boldsymbol{H}_k\boldsymbol{K}_{k-1})^{\mathrm{T}} + \boldsymbol{H}_k\boldsymbol{P}_{k-1}\boldsymbol{H}_k^{\mathrm{T}}\right] \end{cases} \quad (9)$$

Among them, $\boldsymbol{v}_k$ is the difference between the measured value and the predicted value of the residuals. $\boldsymbol{P}_{k/k-1}$ is the predicted covariance matrix. $\boldsymbol{K}_k$ is the optimal Kalman gain. The state equation and measurement equation of the attitude angle as well as the equation of state and the measurement equation of the space position are substituted into equation (9), and then iterative calculation. The multi-sensor data fusion is completed, the navigation information is obtained.

MSNU data fusion results are shown in FIGURE 10. The MSNU is fixed on the turntable, with the roll angle of the angular motion tracking (as shown in FIGURE 10(a)) results showing that the fusion results are basically consistent with the turntable movement posture. There will be some error in the large angle motion, but its precision can satisfy the demand. When the aircraft is hovering, GPS original location information and the location information of the fused result are as shown in FIGURE 10(b). The original location error is around 2.5 m (relative error for a short time), and the location error is about 1.2 m. The fusion algorithm improves the location accuracy significantly.

B. FAULT OBSERVER BASED ON EKF

According to the structural characteristics of the Hex-Rotor UAV, ignoring the influence of the torsional moment on control torque of the roll and pitch channel, the inertia moment of the rotor is also ignored. If each rotor's speed is regarded as an input of the dynamic model of the Hex-Rotor UAV, then the dynamic model of Hex-Rotor UAV is as follows [37]:

$$\begin{cases} \dot{\boldsymbol{\eta}} = \boldsymbol{T} \cdot \boldsymbol{\omega} \\ \boldsymbol{J} \cdot \dot{\boldsymbol{\omega}} = -\boldsymbol{S}(\boldsymbol{\omega})\boldsymbol{J}\boldsymbol{\omega} + \boldsymbol{M} \end{cases} \quad (10)$$

$$\begin{cases} \dot{\boldsymbol{P}} = \boldsymbol{R}_{b-e} \cdot \boldsymbol{V} \\ \dot{\boldsymbol{V}} = -\boldsymbol{S}(\boldsymbol{\omega})\boldsymbol{V} + diag\left(\frac{1}{m}, \frac{1}{m}, \frac{1}{m}\right)\boldsymbol{F} \end{cases} \quad (11)$$

where $\boldsymbol{\eta} = \left[\dot{\phi}, \dot{\theta}, \dot{\psi}\right]^T$ is the Euler angular velocity, $\boldsymbol{\omega} = [p, q, r]^{\mathrm{T}}$ is the angular velocity of the aircraft rotating around each axis relative to the body coordinate system, and $\boldsymbol{T}$ is the rotation velocity to the Euler angular velocity matrix in the body coordinate system, and $T = \begin{bmatrix} \sqrt{3}/2 & 1/2 & 0 \\ -1/2 & \sqrt{3}/2 & 0 \\ 0 & 0 & 1 \end{bmatrix}$. $\boldsymbol{S}$ is the rotation matrix of body coordinate system relative to inertial coordinate system, and $\boldsymbol{S}(\boldsymbol{\omega}) = \begin{bmatrix} 0 & -r & q \\ r & 0 & -p \\ -q & p & 0 \end{bmatrix}$.

$$\begin{bmatrix} M_x \\ M_y \\ M_z \end{bmatrix} = \begin{bmatrix} {}^1\!/\!_2 L\cos\gamma\left(-k_1\Omega_1^2 - 2k_2\Omega_2^2 - k_3\Omega_3^2 + k_4\Omega_4^2 + 2k_5\Omega_5^2 + k_6\Omega_6^2\right) \\ \sqrt{3}/2 L\cos\gamma\left(-k_1\Omega_1^2 + k_3\Omega_3^2 + k_4\Omega_4^2 - k_6\Omega_6^2\right) \\ L\sin\gamma\left(k_1\Omega_1^2 - k_2\Omega_2^2 + k_3\Omega_3^2 - k_4\Omega_4^2 + k_5\Omega_5^2 - k_6\Omega_6^2\right) \end{bmatrix} + \begin{bmatrix} 0 \\ 0 \\ \cos\gamma\,(L_{a1} - L_{a2} + L_{a3} - L_{a4} + L_{a5} - L_{a6}) \end{bmatrix} \tag{12}$$

$$\begin{bmatrix} F_x \\ F_y \\ F_z \end{bmatrix} = \begin{bmatrix} 1/2\sin\gamma\left(k_1\Omega_1^2 - 2k_2\Omega_2^2 + k_3\Omega_3^2 + k_4\Omega_4^2 - 2k_5\Omega_5^2 + k_6\Omega_6^2\right) + G\sin\theta \\ \sqrt{3}/2\sin\gamma\left(k_1\Omega_1^2 - k_3\Omega_3^2 + k_4\Omega_4^2 - k_6\Omega_6^2\right) - G\cos\theta\sin\phi \\ \cos\gamma\left(k_1\Omega_1^2 + k_2\Omega_2^2 + k_3\Omega_3^2 + k_4\Omega_4^2 + k_5\Omega_5^2 + k_6\Omega_6^2\right) - G\cos\theta\cos\phi \end{bmatrix} \tag{13}$$

$\boldsymbol{J} = diag\left(I_x, I_y, I_z\right)$, I_x, I_y, I_z are the moments of inertia for each axis of the aircraft. $P = [x, y, z]^{\mathrm{T}}$ is the position of the aircraft in the inertial coordinate system. $\boldsymbol{V} = [u, v, w]^{\mathrm{T}}$ is the projection of the flight velocity in the body coordinate system. $\boldsymbol{R}_{b-e}$ is the transformation matrix of frame to inertial frame.

$\boldsymbol{M} = [M_x, M_y, M_z]^{\mathrm{T}}$ is the control attitude moment of the aircraft, in which M_x, M_y, M_z represent the control moment of rolling angle, pitch angle, and yaw angle, respectively, and (12), as shown at the top of this page.

$\boldsymbol{F} = [F_x, F_y, F_z]^{\mathrm{T}}$ is the resultant force of the aircraft, namely (13), as shown at the top of this page.

Among them, Ω_1, Ω_2, …, Ω_6 is the rotor speed of each rotor. k_i $(i = 1, 2, \cdots, 6)$ is the actual lifting factor for the i-th actuator. L_{a1}, L_{a2}, …, L_{a6} is the anti-torsional moment of each actuator, and $\boldsymbol{L}_a = (-1)^{i-1}\bar{k}_L\boldsymbol{\Omega}^2 (i = 1, 2, \cdots, 6)$. $\bar{k}_L$ is known as the anti-torsional moment factor.

Therefore, the state equation and observation equation of Hex-Rotor UAV are:

$$\dot{\boldsymbol{X}} = f\left(\boldsymbol{X}, \boldsymbol{U}\right) + \boldsymbol{W} \tag{14}$$

$$\boldsymbol{Z} = \boldsymbol{h}\left(\boldsymbol{X}\right) + \boldsymbol{V} \tag{15}$$

where $f(\boldsymbol{X}, \boldsymbol{U})$ is a nonlinear function set of state vector and control input vector. $\boldsymbol{W}$ is a zero mean random noise vector. $\boldsymbol{V}$ is an observation noise vector. $\boldsymbol{U} = [\hat{k}_1, \hat{k}_2, \cdots, \hat{k}_6]^{\mathrm{T}}$ is an input vector. $\boldsymbol{X} = [\hat{p}, \hat{q}, \hat{r}, \hat{a}_x, \hat{a}_y, \hat{a}_z]^{\mathrm{T}}$ is a state vector. $\boldsymbol{Z} = [p, q, r, a_x, a_y, a_z]^{\mathrm{T}}$ is an observation vector. $[a_x, a_y, a_z]^{\mathrm{T}}$ can be obtained by:

$$\begin{cases} a_x = \left(\dot{u} - r\cdot v + q\cdot w\right) - G\sin\theta/m \\ a_y = \left(\dot{v} - p\cdot w + r\cdot u\right) + G\cos\theta\sin\phi/m \\ a_z = \left(\dot{w} - q\cdot u + p\cdot v\right) + G\cos\theta\cos\phi/m \end{cases} \tag{16}$$

where G represents the local gravity acceleration.

Equations (14) equation (15) are discretized, and the Taylor expansion is used to linearize:

$$\boldsymbol{X}_k = \boldsymbol{\Phi}_{k,k-1}\boldsymbol{X}_{k-1} + \boldsymbol{\Gamma}_{k,k-1}\left(\boldsymbol{U}_{k-1} + \boldsymbol{W}_{k-1}\right) \tag{17}$$

$$\boldsymbol{Z}_k = \boldsymbol{H}_k\boldsymbol{X}_k + \boldsymbol{V}_k, \tag{18}$$

where $\boldsymbol{H}_k = diag\left(1, 1, \cdots, 1\right)$. $\boldsymbol{Z}_k$ comes from the measurement of the gyroscope and accelerometer, and T_s is the sampling interval. The discrete transfer matrix is $\boldsymbol{\Phi}_{k,k-1} = \boldsymbol{\kappa}_{6\times6} + \boldsymbol{F}_k T_s$, and $\boldsymbol{\kappa}_{6\times6} = diag\left(1, 1, 1, 0, 0, 0\right)$. F_k can be solved by the following formula:

$$\boldsymbol{F}_{k,k-1} = \begin{bmatrix} 0 & (I_y - I_z)r(k)/I_x & (I_y - I_z)q(k)/I_x & \\ (I_z - I_x)r(k)/I_y & 0 & (I_z - I_x)p(k)/I_y & 0_{3\times3} \\ (I_x - I_y)q(k)/I_z & (I_x - I_y)p(k)/I_z & 0 & \\ & 0_{3\times3} & & 0_{3\times3} \end{bmatrix} \tag{19}$$

$\boldsymbol{\Gamma}_{k,k-1}$ is the discrete control input matrix, and (20), as shown at the top of the next page, where $\chi_i = \hat{k}_{Li}/k_i$. The lift factor $\hat{k}_i$ is included in the state vector, and the state vector of the augmented fault observer is as follows:

$$\bar{\boldsymbol{X}}_i = \begin{bmatrix} X_i \\ \hat{k}_i \end{bmatrix} \tag{21}$$

The state equation of the augmented state vector $\bar{X}_i$ is as follows:

$$\bar{\boldsymbol{X}}_{i.k} = \bar{\boldsymbol{\Phi}}_{i.k,k-1}\bar{\boldsymbol{X}}_{i.k-1} + \bar{\boldsymbol{\Gamma}}_{i.k,k-1}\left(\boldsymbol{U}_k + \bar{\boldsymbol{W}}_{k-1}\right) \tag{22}$$

$$\boldsymbol{Z}_{i.k} = \bar{\boldsymbol{H}}_{i.k}\bar{\boldsymbol{X}}_{i.k} + \boldsymbol{V}_k \tag{23}$$

Among them, the augmented discrete transfer matrix is:

$$\bar{\boldsymbol{\Phi}}_{i.k,k-1} = \begin{bmatrix} \Phi_{k,k-1} & \Gamma_{k,k-1}^{(j)} \\ 0 & 1 \end{bmatrix} \tag{24}$$

$\Gamma_{k,k-1}^{(j)}$ is the j-th column of controls input matrix $\Gamma_{k,k-1}$. The augmented control input matrix is:

$$\bar{\boldsymbol{\Gamma}}_{i.k,k-1} = \begin{bmatrix} \Gamma_{k,k-1}^{(0,j)} \\ 0 \end{bmatrix} \tag{25}$$

$\Gamma_{k,k-1}^{(0,j)}$ is the j-th column of controls input matrix $\Gamma_{k,k-1}$:

$$\bar{\boldsymbol{H}}_{i,k} = \begin{bmatrix} H_k & 0 \end{bmatrix} \tag{26}$$

Using the s-weighted attenuation memory KF algorithm [39], the failure observer of the$i$-th actuator is obtained:

$$\begin{cases} \hat{\boldsymbol{X}}_{k/k-1} = \boldsymbol{\Phi}_{k/k-1}\hat{\boldsymbol{X}}_{k-1} + \boldsymbol{\Gamma}_{k,k-1}\dot{\boldsymbol{X}}_{k-1} \\ \hat{\boldsymbol{X}}_k = \hat{\boldsymbol{X}}_{k/k-1} + \boldsymbol{K}_k\left(\boldsymbol{Z}_k - \boldsymbol{H}_k\hat{\boldsymbol{X}}_{k/k-1}\right) \\ \boldsymbol{K}_k = \boldsymbol{P}_k\boldsymbol{H}_k^{\mathrm{T}}\left[\boldsymbol{H}_k\boldsymbol{P}_{k/k-1}\boldsymbol{H}_k^{\mathrm{T}} + \boldsymbol{R}_k\right]^{-1} \\ \boldsymbol{P}_{k/k-1} = S\boldsymbol{\Phi}_{k/k-1}\boldsymbol{P}_{k-1}\boldsymbol{\Phi}_{k/k-1}^{\mathrm{T}} + \boldsymbol{\Gamma}_{k,k-1}\boldsymbol{Q}_{k-1}\boldsymbol{\Gamma}_{k,k-1}^{\mathrm{T}} \\ \boldsymbol{P}_k = \left(\boldsymbol{I} - \boldsymbol{K}_k\boldsymbol{H}_k\right)\boldsymbol{P}_{k/k-1}\left(\boldsymbol{I} - \boldsymbol{K}_k\boldsymbol{H}_k\right)^{\mathrm{T}} + \boldsymbol{K}_k\boldsymbol{R}_k\boldsymbol{K}_k^{\mathrm{T}} \end{cases} \tag{27}$$

$$\boldsymbol{\Gamma}_{k,k-1} = \begin{bmatrix} -\frac{L\Omega_1^2 T_s cos\gamma}{2I_x} & -\frac{L\Omega_2^2 T_s cos\gamma}{I_x} & -\frac{L\Omega_3^2 T_s cos\gamma}{2I_x} & \frac{L\Omega_4^2 T_s cos\gamma}{2I_x} & \frac{L\Omega_5^2 T_s cos\gamma}{I_x} & \frac{L\Omega_6^2 T_s cos\gamma}{2I_x} \\ -\frac{\sqrt{3}L\Omega_1^2 T_s cos\gamma}{2I_y} & 0 & \frac{\sqrt{3}L\Omega_3^2 T_s cos\gamma}{2I_y} & \frac{\sqrt{3}L\Omega_5^2 T_s cos\gamma}{2I_y} & 0 & -\frac{\sqrt{3}L\Omega_6^2 T_s cos\gamma}{2I_y} \\ \frac{\Omega_1^2 T_s(L\sin\gamma+\chi_1\cos\gamma)}{I_z} & -\frac{\Omega_2^2 T_s(L\sin\gamma+\chi_2\cos\gamma)}{I_z} & \frac{\Omega_3^2 T_s(L\sin\gamma+\chi_3\cos\gamma)}{I_z} & -\frac{\Omega_4^2 T_s(L\sin\gamma+\chi_4\cos\gamma)}{I_z} & \frac{\Omega_5^2 T_s(L\sin\gamma+\chi_5\cos\gamma)}{I_z} & -\frac{\Omega_6^2 T_s(L\sin\gamma+\chi_6\cos\gamma)}{I_z} \\ \frac{\Omega_1^2\sin\gamma}{2m} & -\frac{\Omega_2^2\sin\gamma}{m} & \frac{\Omega_3^2\sin\gamma}{2m} & -\frac{\Omega_4^2\sin\gamma}{2m} & \frac{\Omega_5^2\sin\gamma}{m} & -\frac{\Omega_6^2\sin\gamma}{2m} \\ \frac{\sqrt{3}\Omega_1^2\sin\gamma}{2m} & 0 & -\frac{\sqrt{3}\Omega_3^2\sin\gamma}{2m} & \frac{\sqrt{3}\Omega_4^2\sin\gamma}{2m} & 0 & -\frac{\sqrt{3}\Omega_6^2\sin\gamma}{2m} \\ \frac{\Omega_1^2\cos\gamma}{m} & \frac{\Omega_2^2\cos\gamma}{m} & \frac{\Omega_3^2\cos\gamma}{m} & \frac{\Omega_4^2\cos\gamma}{m} & \frac{\Omega_5^2\cos\gamma}{m} & \frac{\Omega_6^2\cos\gamma}{m} \end{bmatrix} \tag{20}$$

$$\boldsymbol{B} = \begin{bmatrix} -\frac{lcos\gamma}{2I_x} & -\frac{lcos\gamma}{I_x} & -\frac{lcos\gamma}{2I_x} & \frac{lcos\gamma}{2I_x} & \frac{lcos\gamma}{I_x} & \frac{lcos\gamma}{2I_x} \\ -\frac{\sqrt{3}lcos\gamma}{2I_y} & 0 & \frac{\sqrt{3}lcos\gamma}{2I_y} & \frac{\sqrt{3}lcos\gamma}{2I_y} & 0 & -\frac{\sqrt{3}lcos\gamma}{2I_y} \\ \frac{l\sin\gamma+\chi_1\cos\gamma}{I_z} & -\frac{l\sin\gamma+\chi_2\cos\gamma}{I_z} & \frac{l\sin\gamma+\chi_3\cos\gamma}{I_z} & -\frac{l\sin\gamma+\chi_4\cos\gamma}{I_z} & \frac{l\sin\gamma+\chi_5\cos\gamma}{I_z} & -\frac{l\sin\gamma+\chi_6\cos\gamma}{I_z} \end{bmatrix}$$

According to the second order norm of the fault observer residual vector, we can tell whether the current observation value k is accurate. If the second order norm of the residual vector is less than some constant in a period of time, the current estimate of the lift factor $\hat{k}_i$ can be considered accurate. Then the damage ratio coefficient β_i of the actuator is obtained as follows:

$$\beta_i = 1 - \hat{k}_i \Big/ \bar{k}_i \tag{28}$$

where lift factor $\hat{k}_i$ is estimated by the fault observer, the lift factor $\bar{k}_i$ is measured at the standard atmospheric pressure indoors. Finally, the self-reconfigurable controller will determine whether the current actuator has no fault occurrence according to the value of β_i. The self-reconfigurable controller is used when a fault occurs, and the related parameters in the controller are corrected when there is no fault.

C. SELF-RECONFIGURABLE CONTROLLER DESIGN

The self-reconfigurable controller will decide whether the current actuator is malfunctioning or what the type of fault is according to the value of β_i, making the corresponding fault-tolerant reconstruction when there is a fault, and modifying the relevant parameters in the controller when there is no fault. From the observation information provided by the FDR system, the β_i of each rotor is known. The damage ratio coefficient matrix $\boldsymbol{\beta}$ is described as:

$$\boldsymbol{\beta} = diag\left(1-\beta_1, 1-\beta_2 \cdots, 1-\beta_6\right) \tag{29}$$

The matrix $\boldsymbol{\beta}$ indicates the degree of variation of the lift factor $\hat{k}_i$ estimated by the fault observer group and the variation of the lift factor $\bar{k}_i$ measured at atmospheric pressure.

Considering that the aircraft is usually in a small angular motion state, the rate of change of attitude angle $\dot{\eta}$ is approximately equal to the angular velocity ω of the aircraft, namely $\boldsymbol{T} \approx diag(1, 1, 1)$. With the combination of Equation (28), the attitude control model of the aircraft in fault conditions can be described as:

$$\ddot{\boldsymbol{\eta}} = F\left(\dot{\boldsymbol{\eta}}, t\right) + \boldsymbol{B}\boldsymbol{K}_\beta \boldsymbol{\Omega}^2 \tag{30}$$

where, $\boldsymbol{K}_\beta = \boldsymbol{\beta} \cdot \bar{\boldsymbol{K}}$, $\bar{\boldsymbol{K}}$ is the matrix which composed of lift factors measured at indoor standard atmospheric pressure, and $\bar{\boldsymbol{K}} = diag(\bar{k}_1, \cdots, \bar{k}_6)^{\mathrm{T}}$, $\boldsymbol{\eta} = [\phi, \theta, \psi]^{\mathrm{T}}$ is the attitude angle, and $\boldsymbol{\Omega}^2 = [\Omega_1^2, \Omega_2^2, \Omega_3^2, \Omega_4^2, \Omega_5^2, \Omega_6^2]^{\mathrm{T}}$ is the rotor speed vector. The expression of the control input matrix $\boldsymbol{B}$, as shown at the top of this page.

Taking actuator 1 as an example, other actuator processes proceed in a similar way. Assuming that there is a gain fault in actuator 1, the pseudo-inverse algorithm is used to solve the desired rotational speed of the rotor, that is:

$$\boldsymbol{\Omega}_d^2 = \hat{\boldsymbol{K}}^{-1}\left(\boldsymbol{B}_{4\times 6}\right)^{-1}\begin{bmatrix} \boldsymbol{M}_d \\ F_z \end{bmatrix} \tag{31}$$

where $\boldsymbol{B}_{4\times 6}$ is an augmented matrix of the control input matrix $\boldsymbol{B}$. $\boldsymbol{M}_d = [M_x, M_y, M_z]^{\mathrm{T}}$ is the desired control moment to maintain a stable attitude. F_z is the desired lift. Substituting the relevant parameters in TABLE 1 to $\hat{\boldsymbol{K}}^{-1}\left(\boldsymbol{B}_{4\times 6}\right)^{-1}$, we have (32), as shown at the top of the next page.

$$\hat{\boldsymbol{K}}^{-1}\left(\boldsymbol{B}_{4\times6}\right)^{-1}=\begin{bmatrix}-0.0715/(1-\beta_1) & -0.124/(1-\beta_1) & 0.569/(1-\beta_1) & 0.584/(1-\beta_1)\\ -0.143 & 0 & -0.569 & 0.584\\ -0.0715 & 0.124 & 0.569 & 0.584\\ 0.0715 & 0.124 & -0.569 & 0.584\\ 0.143 & 0 & 0.569 & 0.584\\ 0.0715 & -0.124 & -0.569 & 0.584\end{bmatrix}\times 10^3 \tag{32}$$

According to Equation (31), the desired rotation speed of each rotor $\boldsymbol{\Omega}_d^2=\left[\Omega_{1.d}^2,\cdots,\Omega_{6.d}^2\right]^{\mathrm{T}}$ can be obtained. When rotor 1 is unable to achieve the desired speed $\Omega_{1.d}^2$, it can only maintain its maximum speed Ω_1. This shows that the lift provided by rotor 1 decreases, so the lift factor k_1 of rotor 1 in the prototype is reduced. At this moment, the equivalent lift factor $\tilde{k}_1$ is:

$$\tilde{k}_1=\widehat{\Omega}_1^2 k_i \Big/ \Omega_{1.d}^2 \tag{33}$$

When β_1 increases, $\tilde{k}_1$ will decrease. This will affect the stability of the system by increasing the deviation of the lifting factor matrix $\hat{K}$ of the controller and the lifting factor matrix $\tilde{\boldsymbol{K}}=diag\left(\tilde{k}_1,k_2,\cdots,k_6\right)$ of the rotor. The criterion can be given as [36]:

$$\begin{aligned}&\dot{\boldsymbol{V}}_2\\&=-\left\|\boldsymbol{\sigma}^{\mathrm{T}}\right\|\left(\|\boldsymbol{H}\boldsymbol{\alpha}\|-\widehat{\rho}\cdot\widehat{\boldsymbol{\xi}}\cdot\breve{\rho}\left\|\begin{array}{l}\boldsymbol{A}\left(z_2-\boldsymbol{C}z_1\right)+\\ \boldsymbol{F}\left(\dot{\boldsymbol{\eta}},t\right)-\ddot{\boldsymbol{\eta}}_d+\boldsymbol{C}\dot{z}_1\end{array}\right\|\right)\\&\quad-\boldsymbol{Z}^{\mathrm{T}}\boldsymbol{Q}\boldsymbol{Z}\le 0\end{aligned} \tag{34}$$

where $\boldsymbol{H}=diag\left(h_1,h_2,h_3\right)$,$\boldsymbol{\alpha}=[\alpha_1,\alpha_2,\alpha_3]^{\mathrm{T}}$ represents the design parameters of the sliding mode controller. $\widehat{\boldsymbol{\xi}}=\left\|\boldsymbol{I}-\tilde{K}\hat{K}^{-1}\right\|$,$\widehat{\rho}=\sqrt{\lambda_{\max}\left(\boldsymbol{B}^T\boldsymbol{B}\right)}$,$\breve{\rho}=\sqrt{\lambda_{\min}\left(\boldsymbol{B}^T\boldsymbol{B}\right)}$. If the self-reconfigurable controller activated by the gain fault does not satisfy the criterion given by Equation (34), it is considered that the attitude angle control of the aircraft may be unstable, and the corresponding fault actuator will stop working. The processing mode of failure is adopted.

Assuming that a failure occurs in actuator 1, actuator 1 will not generate any lift ($\beta_1=1$). At this time, the control input matrix $\boldsymbol{B}_{4\times6}$ is singular. Reducing the order of $\boldsymbol{B}_{4\times6}$ for a 4×5 matrix $\boldsymbol{B}_{4\times5}$, and introducing the relevant parameters of TABLE 1, the pseudo-inverse matrix $\left(\boldsymbol{B}_{4\times5}\right)^{-1}$ is given as:

$$\begin{aligned}&\hat{\boldsymbol{K}}^{-1}\left(\boldsymbol{B}_{4\times5}\right)^{-1}\\&=\begin{bmatrix}-0.179 & -0.0619 & -0.285 & 0.877\\ -0.107 & 0.0619 & 0.853 & 0.877\\ 0.143 & 0.248 & -1.138 & 0\\ 0.107 & -0.0619 & 0.853 & 0.877\\ 0.0357 & -0.1857 & -0.285 & 0.877\end{bmatrix}\times 10^3\end{aligned} \tag{35}$$

Equation (35) indicates that the desired speed of actuator 4 is very small and may be negative. We change the control input matrix $\boldsymbol{B}_{4\times6}$ to a 3 × 5 matrix $\boldsymbol{B}_{3\times5}$, whose pseudo-inverse matrix $\left(\boldsymbol{B}_{3\times5}\right)^{-1}$ is:

$$\boldsymbol{\Omega}_{(1).d}^2=\hat{\boldsymbol{K}}_{(1)}^{-1}\left(\boldsymbol{B}_{3\times5}\right)^{-1}\begin{bmatrix}M_x\\ M_y\\ F_z\end{bmatrix} \tag{36}$$

where $\boldsymbol{\Omega}_{(1).d}^2=[\Omega_2^2,\Omega_3^2,\Omega_4^2,\Omega_5^2,\Omega_6^2]^{\mathrm{T}}$, $\hat{\boldsymbol{K}}_{(1)}=[\hat{k}_2,\cdots,\hat{k}_6]^{\mathrm{T}}$. The control input matrix $\boldsymbol{B}_{3\times5}$ is:

$$\begin{aligned}&\boldsymbol{B}_{3\times5}\\&=\begin{bmatrix}\dfrac{l\cos\gamma}{I_x} & \dfrac{l\cos\gamma}{2I_x} & \dfrac{l\cos\gamma}{2I_x} & \dfrac{l\cos\gamma}{I_x} & \dfrac{l\cos\gamma}{2I_x}\\ 0 & \dfrac{\sqrt{3}l\cos\gamma}{2I_y} & \dfrac{\sqrt{3}l\cos\gamma}{2I_y} & 0 & -\dfrac{\sqrt{3}l\cos\gamma}{2I_y}\\ \cos\gamma & \cos\gamma & \cos\gamma & \cos\gamma & \cos\gamma\end{bmatrix}\end{aligned} \tag{37}$$

Equation (37) indicates that the asymmetry of the pitch channel and roll channel will lead to the divergence of the controller. Therefore, the coordinate transformation of the Hex-Rotor UAV is needed to redefine the body coordinate system. The coordinate transformation method is as follows: the O_bx_b axis coincides with the connecting rod of actuator 1, pointing outward to be positive. The O_bz_b axis remains the same. The O_by_b axis and the remaining two axes form the right-hand rectangular coordinate system, The control input matrix after coordinate transformation is described as follows:

$$\begin{aligned}&\bar{\boldsymbol{B}}_{3\times5}\\&=\begin{bmatrix}\dfrac{-\sqrt{3}l\cos\gamma}{2I_x} & \dfrac{-\sqrt{3}l\cos\gamma}{2I_x} & 0 & \dfrac{\sqrt{3}l\cos\gamma}{2I_x} & \dfrac{\sqrt{3}l\cos\gamma}{2I_x}\\ \dfrac{-l\cos\gamma}{2I_y} & \dfrac{l\cos\gamma}{2I_y} & \dfrac{l\cos\gamma}{I_y} & \dfrac{l\cos\gamma}{2I_y} & \dfrac{-l\cos\gamma}{2I_y}\\ \cos\gamma & \cos\gamma & \cos\gamma & \cos\gamma & \cos\gamma\end{bmatrix}\end{aligned} \tag{38}$$

The inversion sliding mode controller designed for attitude stability control is as follows:

$$\begin{aligned}&\boldsymbol{U}\\&=\left(\hat{\boldsymbol{K}}_{(1).d}\right)^{-1}\left(\bar{\boldsymbol{B}}_{3\times5}\right)^{-1}\\&\quad\times\begin{pmatrix}-\boldsymbol{A}_{(1)}\left(z_{(1).2}-\boldsymbol{C}_{(1)}z_{(1).1}\right)-\boldsymbol{F}_{(1)}\left(\dot{\boldsymbol{\eta}}_{(1)},t\right)+\ddot{\boldsymbol{\eta}}_{(1).d}\\ -\boldsymbol{C}_{(1)}\dot{z}_{(1).1}-\boldsymbol{H}_{(1)}\left(\boldsymbol{\sigma}_{(1)}+\boldsymbol{\alpha}_{(1)}\mathrm{sgn}\left(\sigma\right)\right)\end{pmatrix}\end{aligned} \tag{39}$$

where $\boldsymbol{A}_{(1)}$, $\boldsymbol{C}_{(1)}$, $\boldsymbol{H}_{(1)}$ represent the reduced order matrix. $z_{(1).2},z_{(1).1},\boldsymbol{F}_{(1)}\left(\dot{\boldsymbol{\eta}}_{(1)},t\right)$ represents the reduced order vector.

$\dot{\boldsymbol{\eta}}_{(1)}$, $\boldsymbol{\eta}_{(1)}$ is the feedback after coordinate transformation and in descending order. Defining state variables $\boldsymbol{Z}_{(1)} = [z_{(1).2}, z_{(1).1}]^{\boldsymbol{T}}$ proceeds as follows:

$$\begin{aligned}\dot{\boldsymbol{V}}_2 &\leq -\left\|\boldsymbol{\sigma}_{(1)}^{\mathrm{T}}\right\| \\ &\times \left(\left\|\boldsymbol{H}_{(1)}\boldsymbol{\alpha}_{(1)}\right\| - \left\|\left(\bar{\boldsymbol{B}}_{3\times5}\right)\left(I - \boldsymbol{K}_{(1)}\hat{\boldsymbol{K}}_{(1)}^{-1}\right)\left(\bar{\boldsymbol{B}}_{3\times5}\right)^{-1}\right\| \right. \\ &\times \left. \left\| \begin{matrix} \boldsymbol{A}_{(1)}\left(z_{(1).2} - \boldsymbol{C}_{(1)}z_{(1).1}\right) - \ddot{\boldsymbol{\eta}}_{(1).d} \\ +\boldsymbol{F}_{(1)}\left(\dot{\boldsymbol{\eta}}_{(1)}, t\right) + \boldsymbol{C}_{(1)}\dot{z}_{(1).1} \end{matrix} \right\| \right) \\ &- \boldsymbol{Z}_{(1)}^{\mathrm{T}}\boldsymbol{Q}_{4\times4}\boldsymbol{Z}_{(1)} \end{aligned} \tag{40}$$

where, $\boldsymbol{Q}$, $\boldsymbol{N}$, $\boldsymbol{K}_{(1)}\hat{\boldsymbol{K}}_{(1)}^{-1}$, and Δk_i, as shown at the bottom of this page.

The matrix $\boldsymbol{H}_{(1)}$ is constructed such that $\bar{\boldsymbol{B}}_{3\times5}\boldsymbol{K}_{(1)}\hat{\boldsymbol{K}}_{(1)}^{-1}\left(\bar{\boldsymbol{B}}_{3\times5}\right)^{-1}\boldsymbol{H}_{(1)}$ is a symmetrical matrix. Supposing that $R_i(i = 1, 2)$ is the principal minors of $\bar{\boldsymbol{B}}_{3\times5}\boldsymbol{K}_{(1)}\hat{\boldsymbol{K}}_{(1)}^{-1}\left(\bar{\boldsymbol{B}}_{3\times5}\right)^{-1}\boldsymbol{H}_{(1)}$, we have:

$$R_1 = \sum_{i\neq1,4}^{6} 0.25\Delta k_i > 0 \tag{41}$$

$$R_2 = \sum_{i=2}^{5}\left(\sum_{j>i,j\neq i+3}^{6} 0.125\Delta k_i\Delta k_j\right) > 0 \tag{42}$$

Through Equations (41) and (42), it is proven that $\bar{\boldsymbol{B}}_{3\times5}\boldsymbol{K}_{(1)}\hat{\boldsymbol{K}}_{(1)}^{-1}\left(\bar{\boldsymbol{B}}_{3\times5}\right)^{-1}\boldsymbol{H}_{(1)}$ must be positive and definite. It can be further obtained:

$$\dot{\boldsymbol{V}}_2 \leq -\left\|\boldsymbol{H}_{(1)}\boldsymbol{\alpha}_{(1)}\right\|\left\|\boldsymbol{\sigma}_{(1)}^{\mathrm{T}}\right\| - \boldsymbol{Z}_{(1)}^{\mathrm{T}}\boldsymbol{Q}_{4\times4}\boldsymbol{Z}_{(1)} \leq 0 \tag{43}$$

According to the LaSalle invariance theorem, when $\dot{\boldsymbol{V}}_2 \equiv 0$, and then $z_{(1)} \equiv 0$, $\boldsymbol{\sigma}_{(1)} \equiv 0$. when $t \to \infty$, we have $z_{(1)} \to \infty$, $\boldsymbol{\sigma}_{(1)} \to \infty$. So the system tracking error $z_{(1).1} \to 0$, $z_{(1).2} \to 0$. The accuracy of tracking depends on the real-time estimation accuracy of each rotor lifting factor k_i.

The stability of the closed-loop system under the self-reconfigurable control strategy, That is, the stability of the reconfigured dynamic inverse controller. Generally, the

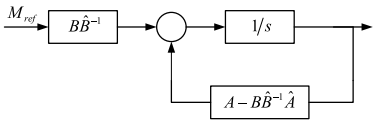

FIGURE 11. Closed-loop transfer function of the imperfect dynamic inversion controller.

closed-loop transfer function of the imperfect dynamic inversion controller can be expressed as follows:

Considering that the aircraft is usually in a small angle motion state, it is considered that the attitude angle change rate $\dot{\eta}$ is approximately equal to the angular velocity ω of the aircraft. The linearized attitude rotation dynamic model of the Hex-Rotor UAV is obtained, that is:

$$\begin{cases} \dot{\boldsymbol{\omega}} = \boldsymbol{A}\boldsymbol{\omega}(t) + \boldsymbol{B}\boldsymbol{\Omega}^2(t) \\ \boldsymbol{y} = \boldsymbol{\omega}(t) \end{cases} \tag{44}$$

Among them, $\boldsymbol{A}$ and $\boldsymbol{B}$ are respectively state transition matrix and control input matrix.

Define $\boldsymbol{B}_{DI} = \boldsymbol{B}\hat{\boldsymbol{B}}^{-1}$, $\boldsymbol{A}_{DI} = \boldsymbol{A} - \boldsymbol{B}\hat{\boldsymbol{B}}^{-1}\hat{\boldsymbol{A}}$.

a: STABILITY PROOF AFTER GAIN FAULT OCCURS

Assuming that the gain fault occurs in actuator 1, the following results are obtained in (45), as shown at the bottom of this page.

Because the lifting factor with the same parameters is used to extend the Kalman observer, It can be considered that, at the same time, the relative error of lifting factor estimation of no fault actuator is similar to that of lifting factor estimation of fault actuator, that is,

$$k \Big/ \hat{k} \approx k_1 \Big/ \hat{k}_1 \tag{46}$$

Combined with equation (44), the input matrix can be simplified to be expressed as:

$$\boldsymbol{B}_{DI} = \begin{bmatrix} \hat{I}_x k \Big/ I_x \bar{k} & 0 & 0 \\ 0 & \hat{I}_y k \Big/ I_y \bar{k} & 0 \\ 0 & 0 & \hat{I}_z k \Big/ I_z \bar{k} \end{bmatrix} \tag{47}$$

$$\boldsymbol{Q} = \begin{bmatrix} \boldsymbol{C}_{(1)} + \boldsymbol{A}_{(1)}^{\mathrm{T}}(\bar{\boldsymbol{B}}_{3\times5})\boldsymbol{K}_{(1)}\hat{\boldsymbol{K}}_{(1)}^{-1}(\bar{\boldsymbol{B}}_{3\times5})^{-1}\boldsymbol{H}_{(1)}\boldsymbol{A}_{(1)} & \boldsymbol{A}_{(1)}^{\mathrm{T}}(\bar{\boldsymbol{B}}_{3\times5})\boldsymbol{K}_{(1)}\hat{\boldsymbol{K}}_{(1)}^{-1}(\bar{\boldsymbol{B}}_{3\times5})^{-1}\boldsymbol{H}_{(1)} - \boldsymbol{N} \\ (\bar{\boldsymbol{B}}_{3\times5})\boldsymbol{K}_{(1)}\hat{\boldsymbol{K}}_{(1)}^{-1}(\bar{\boldsymbol{B}}_{3\times5})^{-1}\boldsymbol{H}_{(1)}\boldsymbol{A}_{(1)} - \boldsymbol{N} & (\bar{\boldsymbol{B}}_{3\times5})\boldsymbol{K}_{(1)}\hat{\boldsymbol{K}}_{(1)}^{-1}(\bar{\boldsymbol{B}}_{3\times5})^{-1}\boldsymbol{H}_{(1)} \end{bmatrix},$$

$$\boldsymbol{N} = diag\left(\frac{1}{2}, \frac{1}{2}, \frac{1}{2}, \frac{1}{2}\right), \quad \boldsymbol{K}_{(1)}\hat{\boldsymbol{K}}_{(1)}^{-1} = diag(\Delta k_1, \cdots, \Delta k_6)^{\mathrm{T}}, \ \Delta k_i = k_i \Big/ \hat{k}_i \in [0.85, 1.15].$$

$$\boldsymbol{B}_{DI} = \begin{bmatrix} \dfrac{0.917\hat{I}_x k}{I_x\hat{k}} + \dfrac{0.083\hat{I}_x k_1}{I_x\hat{k}_1} & -\dfrac{0.141\hat{I}_y k}{I_x\hat{k}} + \dfrac{0.141\hat{I}_y k_1}{I_x\hat{k}_1} & \dfrac{0.268\hat{I}_z k}{I_x\hat{k}} - \dfrac{0.268\hat{I}_z k_1}{I_x\hat{k}_1} \\ -\dfrac{0.148\hat{I}_x k}{I_y\hat{k}} + \dfrac{0.148\hat{I}_x k_1}{I_y\hat{k}_1} & \dfrac{0.75\hat{I}_y k}{I_y\hat{k}} + \dfrac{0.25\hat{I}_y k_1}{I_y\hat{k}_1} & \dfrac{0.474\hat{I}_z k}{I_y\hat{k}} - \dfrac{0.474\hat{I}_z k_1}{I_y\hat{k}_1} \\ \dfrac{0.052\hat{I}_x k}{I_z\hat{k}} - \dfrac{0.052\hat{I}_x k_1}{I_z\hat{k}_1} & \dfrac{0.088\hat{I}_y k}{I_z\hat{k}} - \dfrac{0.088\hat{I}_y k_1}{I_z\hat{k}_1} & \dfrac{0.833\hat{I}_z k}{I_z\hat{k}} + \dfrac{0.167\hat{I}_z k_1}{I_z\hat{k}_1} \end{bmatrix} \tag{45}$$

Further, $\boldsymbol{B}_{DI}\boldsymbol{A}$ is obtained, that is,

$$\boldsymbol{B}_{DI}\boldsymbol{A} = \begin{bmatrix} 0 & k\left(\hat{I}_y - \hat{I}_z\right) r \Big/ \bar{k} I_x & k\left(\hat{I}_y - \hat{I}_z\right) q \Big/ \bar{k} I_x \\ k\left(\hat{I}_z - \hat{I}_x\right) r \Big/ \bar{k} I_y & 0 & k\left(\hat{I}_z - \hat{I}_x\right) p \Big/ \bar{k} I_y \\ k\left(\hat{I}_x - \hat{I}_y\right) q \Big/ \bar{k} I_z & k\left(\hat{I}_x - \hat{I}_y\right) p \Big/ \bar{k} I_z & 0 \end{bmatrix} \tag{48}$$

According to the analysis in section 5.3 of reference [37], the controller converges steadily in this case.

b: STABILITY PROOF AFTER FAILURE OCCURS

Assuming that the failure occurs in actuator 1, the following results are obtained:

$$\boldsymbol{B}_{DI} = \begin{bmatrix} \hat{I}_x k \Big/ I_x \bar{k} & 0 & 0 \\ 0 & \hat{I}_y k \Big/ I_y \bar{k} & 0 \\ 0 & 0 & k \Big/ \bar{k} \end{bmatrix} \tag{49}$$

Further, $\boldsymbol{B}_{DI}\boldsymbol{A}$ is obtained, that is,

$$\boldsymbol{B}_{DI}\boldsymbol{A} = \begin{bmatrix} 0 & k\left(\hat{I}_y - \hat{I}_z\right) r \Big/ \bar{k} I_x & k\left(\hat{I}_y - \hat{I}_z\right) q \Big/ \bar{k} I_x \\ k\left(\hat{I}_z - \hat{I}_x\right) r \Big/ \bar{k} I_y & 0 & k\left(\hat{I}_z - \hat{I}_x\right) p \Big/ \bar{k} I_y \\ 0 & 0 & 0 \end{bmatrix} \tag{50}$$

Due to the structural characteristics of Hex-Rotor UAV, it can be considered that $I_x - I_y \approx 0$. The elements of the first column and the second column of the third row are treated as zero. Similarly, according to the analysis in section 5.3 of reference [37], the controller converges steadily in this case.

IV. NUMERICAL SIMULATION AND FLIGHT EXPERIMENT

In this section, the FOB based on EKF is verified by numerical simulation. In order to speed up the convergence speed of the FOB, the *s*-weighted attenuation memory parameter is added. Which indicates that the weight of the observation value is increased in the filter equation. Conversely, the weight of the observed value in the filter equation is reduced. However, the s-weighted attenuation memory parameter will lead to a large number of burrs of the observed values, and therefore, the value of the s parameter should be considered comprehensively.

The influence experiment of *s*-weighted attenuation memory parameters on the lift factor was investigated, and the value of s parameter was reasonably selected. The experimental results are shown in FIGURE 12.

Suppose the lift factor specified in the aircraft (red, blue, and green curves) and the actual lift factor curve (black) has a certain error, the FOB estimate lift factor since 0.06 s. In FIGURE 12, the result shows that when $s = 1.0$, the lifting factor tracking curve is smooth, but the convergence rate is slow (about 0.2 s). At the time of $s = 1.08$, the lift factor

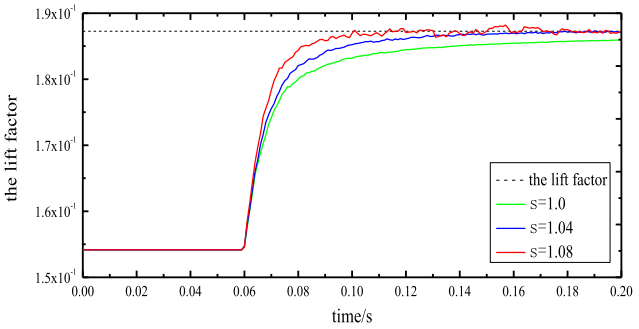

FIGURE 12. Effect of s parameters on fault observer.

tracking curve has more burr, but the convergence rate was fast (about 0.05 s). Although the tracking speed is fast, in the actual system, due to the influence of the sensor noise, its burr is also large and the measurement accuracy is low. According to the above analysis, the weighted attenuation memory parameter $s = 1.04$ is adopted.

The simulation verifies that the lift factor observer group can simultaneously estimate the lifting factor for all the actuators. The simulation background is that the Hex-Rotor UAV is in flight state, and the lift factor in the controller is about 15% error. The experimental results are shown in FIGURE 13. As can be seen from FIGURE 13, the fault observer is activated at 0.03 s, and the lift factor of each actuator estimated by the fault observer is close to the set value. The fault observer group designed in this paper can accurately track the lift factor of each actuator.

Next, the effectiveness of the FOB in the actuator of sudden fault and gradual fault is verified. The experimental results are shown in FIGURE 14. FIGURE 14 shows that actuator 2 has a sudden fault at about 0.1 s, its lift factor fell by about 25%, actuator 2 with fault is located accurately, the value of the lift factor is also estimated by the FOB. In addition, actuator 5 has a gradual fault at about 0.1 s, and the lift factor is decreased at a certain rate. The FOB determines the location of the fault actuator and tracks the lift factors accurately. To sum up, the fault isolation (confirm fault location) and the fault identification (fault size) can be implemented by the designed FOB group. It monitors the health of all actuators of the Hex-Rotor UAV, which provides a solid foundation for the self-reconfigurable controller.

This section will test the stability and control effect of the self-reconfigurable controller in the actual flight of the prototype, as shown in FIGURE 15. The design of the self-reconfigurable controller is based on the sliding mode control method. In the case of gain fault of the actuator, according to equation (34), controller parameters are selected. And in the case of actuator failure, a failure occurs, the controller parameters can be obtained by equation (43). First, the flight experiment of the gain fault of the actuator is carried out. The experimental environment is outdoors, and the wind speed is about 3.2-4 m/s, in the southeast direction. After a gain fault occurs, the lift factor of the actuator decreases, but the effect

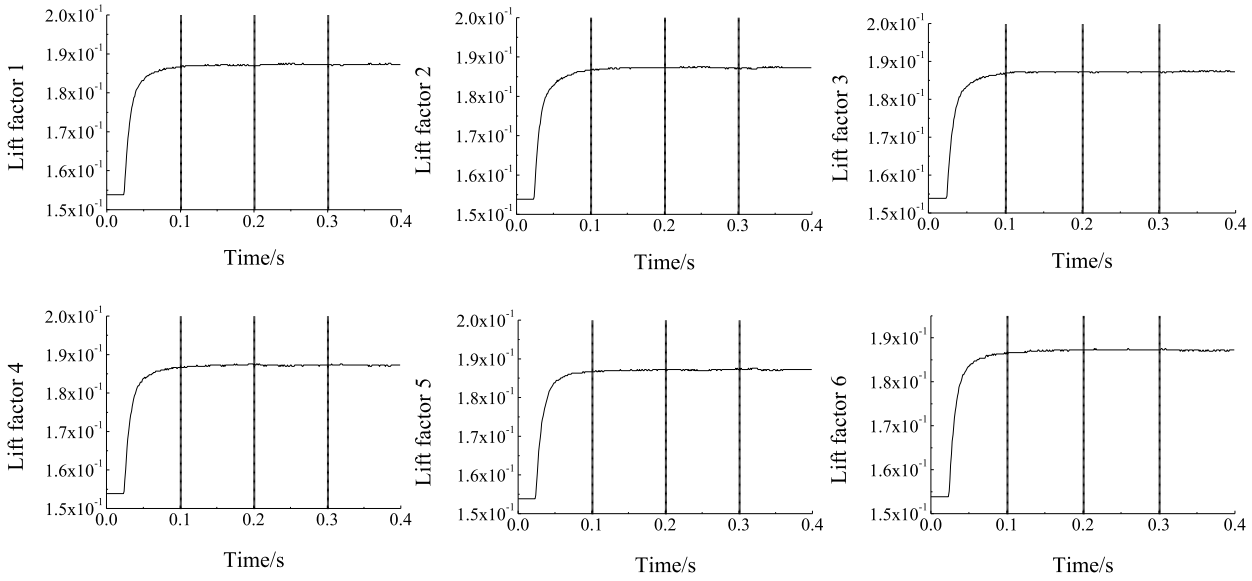

FIGURE 13. Estimation of lift factor for each actuator.

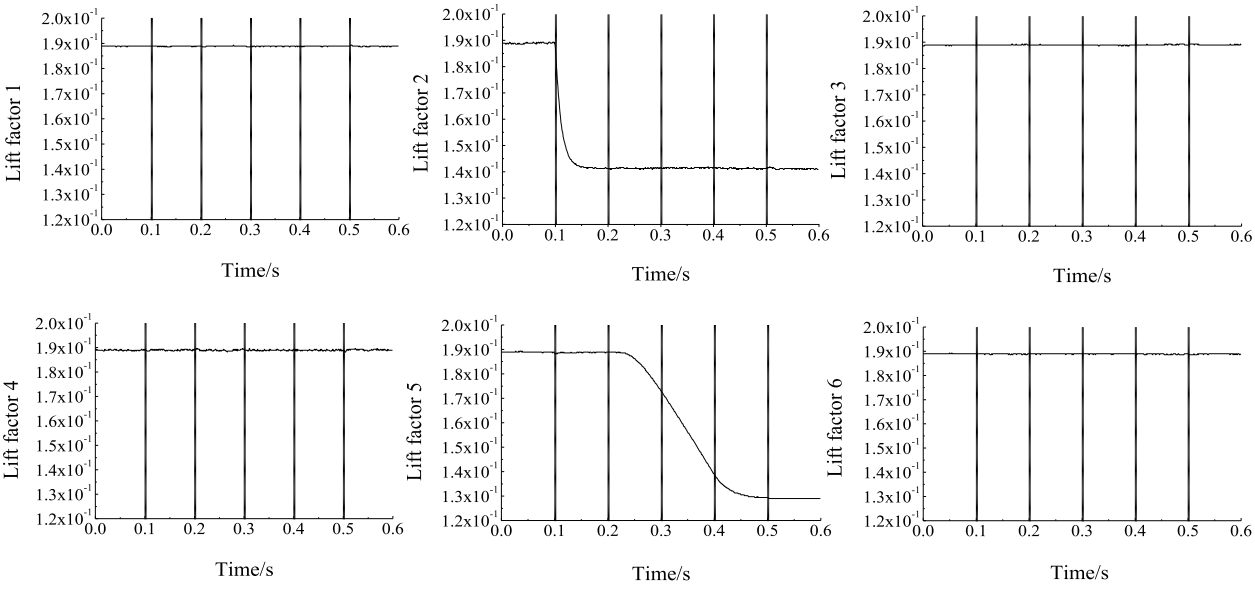

FIGURE 14. Estimation of sudden fault and gradual fault of fault observer group.

FIGURE 15. Flight experiment of Hex-Rotor UAV.

of the decrease in the lift factor could be compensated for by increasing the speed of BLDCM to a certain extent. The experimental results are shown in FIGURE 16.

The results show that actuator 6 has a gain fault around 1.9 s (the lift factor is about 70% of normal value). In FIGURE 16, the red curve is the given value of the attitude angle, the black curve is the actual tracking curve of the attitude angle. It can be seen that the self-reconfigurable controller completes the controller reconstruction through 0.4 s, and restores the attitude angle stability. The controller has certain maneuvering ability and control quality. According to the above analysis, after the gain fault occurs, the stability of the attitude control of the aircraft is guaranteed by the self-reconfigurable controller. The reliability of the aircraft is improved.

Next, the flight experiment of the failure of the actuator is carried out, and the experimental environment is the same as before. After the failure occurs, the actuator completely loses

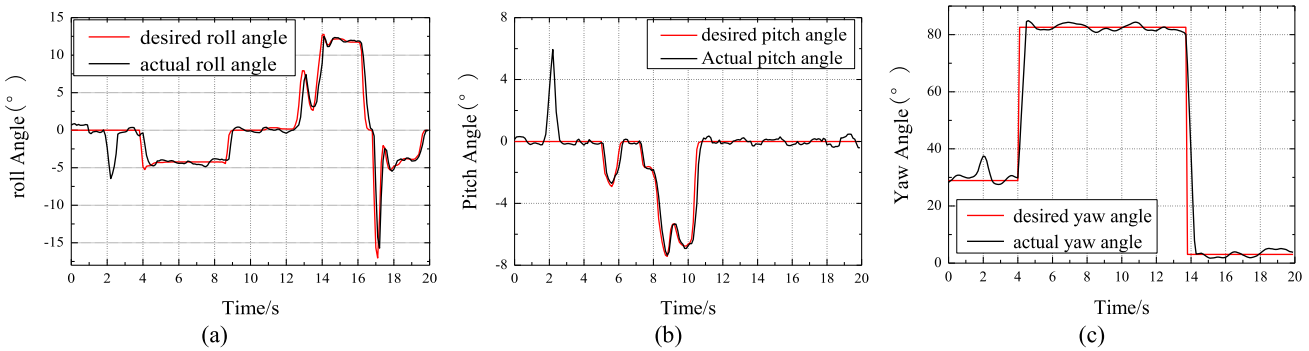

FIGURE 16. Attitude angle tracking curve of gain type fault. (a) Roll angle. (b) Pitch angle. (c) Yaw angle.

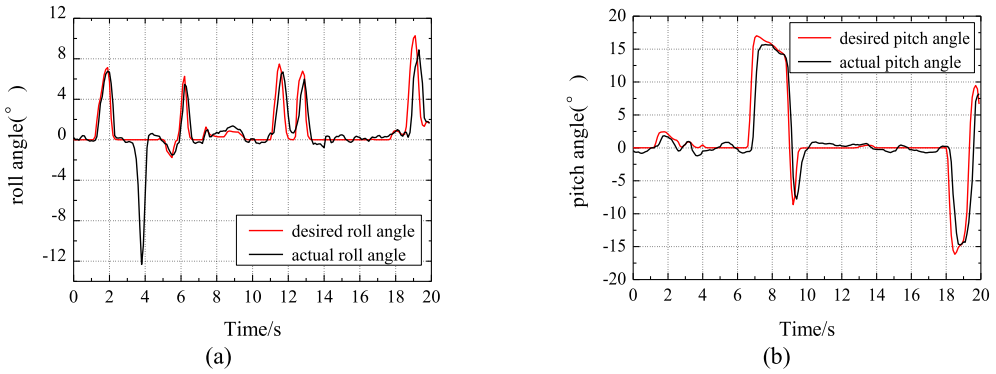

FIGURE 17. Attitude angle tracking curve of failure type fault. (a) Roll angle. (b) Pitch angle.

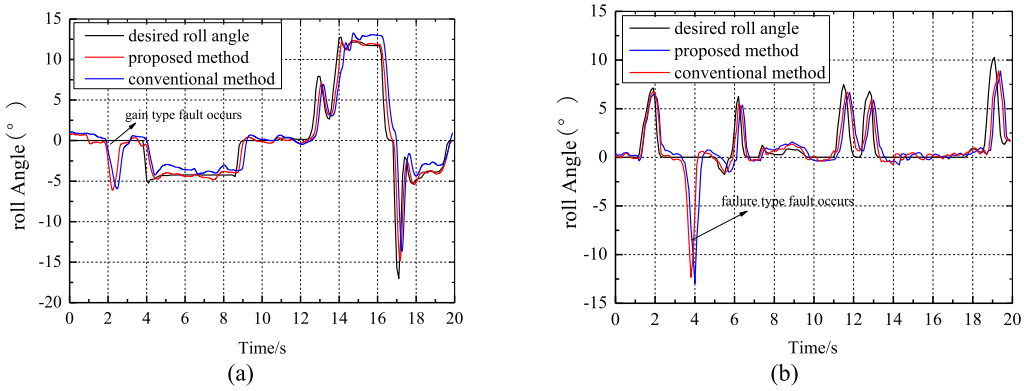

FIGURE 18. Comparison of attitude angle tracking curve of the proposed method and the sliding mode observer. (a) Gain type fault. (b) Failure type fault.

the driving force, and the control input matrix will change. In order to ensure the safety of the aircraft, it is necessary to abandon the control of the yaw angle, and only control the pitch angle, roll angle, and flight height. The experimental results are shown in FIGURE 17.

In FIGURE 17, the red curve is the given value of the roll and pitch angles; the black curve is the actual tracking curve of the attitude angle. FIGURE 17(a) shows that actuator 5 has a failure at 3.5 s, and a complete loss of driving force. This leads to a peak value of 12° appearing on the roll channel in the prototype. At this point, the aircraft is in danger of instability, and the self-reconfigurable controller finally completes the stability control of the roll angle. FIGURE 17(b) shows that actuator 5 does not participate in the control of the pitch angle, but the control effect of the pitch angle decreases due to the coupling relation of the nonlinear system. The experiment proves that the self-reconfigurable controller can guarantee the overall safety of the aircraft.

In order to verify the effectiveness of the proposed method, a comparative experiment with the traditional sliding mode observer method under actuator conditions is carried out. The comparison results of attitude angle tracking are shown in Figure 18. The black curve is the desired roll angle, the red curve is obtained by using the method presented in this paper,

and the blue is curve is obtained by using the conventional method. Form the Figure 18, the conventional method can track the desired roll angle. However, the tracking effect is not ideal, and there are large tracking error. By comparison, the proposed method can track the desired roll angle more accurate, and the tracking error is small.

TABLE 3. Mean values and standard deviation of attitude angle tracking error.

Method	*Fault type*	*Value*	
		Mean value	Standard deviation
Conventional method	gain type fault	1.6229	2.3971
	failure type fault	1.3410	1.9731
Proposed method	gain type fault	0.8811	1.4985
	failure type fault	0.9454	1.6695

The statistical analysis comprising of mean and standard deviation values of the tracking error corresponding to both the conventional method and the proposed FDR schemes are gathered in TABLE 3.

V. CONCLUSIONS

The construction of fast and accurate fault detection and reconstruction is part of the FTC of an unmanned aerial vehicle system and guarantees safe flight in fault conditions. In this paper, fault detection and reconstruction were designed for a Hex-rotor UAV, and a fault detection and reconstruction algorithm based on multi-fault classification was designed. The numerical simulation results show that the designed fault detector set can accurately estimate and track each actuator lift factor and can quickly detect the fault location and type and achieve fault isolation. The actual flight experiment results of the prototype aircraft show that the reconfiguration controller can guarantee the attitude control stability and control quality of the Hex-Rotor UAV after the gain fault and failure occurred in actuator, and effectively improve the reliability, and security of the aircraft.

REFERENCES

[1] M. Hassanalian and A. Abdelkefi, "Classifications, applications, and design challenges of drones: A review," *Prog. Aerosp. Sci.*, vol. 91, pp. 99–131, May 2017.

[2] Y. Zhong, Y. Zhang, W. Zhang, J. Zuo, and H. Zhan, "Robust actuator fault detection and diagnosis for a quadrotor UAV with external disturbances," *IEEE Access*, vol. 6, pp. 48169–48180, 2018.

[3] D.-T. Nguyen, D. Saussie, and L. Saydy, "Quaternion-based robust fault-tolerant control of a quadrotor UAV," in *Proc. Int. Conf. Unmanned Aircr. Syst. (ICUAS)*, Miami, FL, USA, Jun. 2017, pp. 1333–1342.

[4] F. Chen, J. Niu, and G. Jiang, "Nonlinear fault-tolerant control for hypersonic flight vehicle with multi-sensor faults," *IEEE Access*, vol. 6, pp. 25427–25436, 2018.

[5] D. Vey and J. Lunze, "Experimental evaluation of an active fault-tolerant control scheme for multirotor UAVs," in *Proc. 3rd Conf. Control Fault-Tolerant Syst. (SysTol)*, Barcelona, Spain, Sep. 2016, pp. 125–132.

[6] F. Bateman, H. Noura, and M. Ouladsine, "An actuator fault detection, isolation and estimation system for an UAV using input observers," in *Proc. ECC*, Kos, Greece, Jul. 2007, pp. 1805–1810.

[7] Z. Gao, Z. Zhou, G. Jiang, M. Qian, and J. Lin, "Active fault tolerant control scheme for satellite attitude systems: Multiple actuator faults case," *Int. J. Control, Autom. Syst.*, vol. 16, no. 4, pp. 1794–1804, Aug. 2018.

[8] X. Zhang, F. Zhu, and S. Guo, "Actuator fault detection for uncertain systems based on the combination of the interval observer and asymptotical reduced-order observer," *Int. J. Control*, vol. 92, pp. 1–20, May 2019. doi: 10.1080/00207179.2019.1620329.

[9] S. Zeghlache, D. Saigaa, and K. Kara, "Fault tolerant control based on neural network interval type-2 fuzzy sliding mode controller for octorotor UAV," (in Chinese) *Frontiers Comput. Sci.*, vol. 10, pp. 657–672, Aug. 2016.

[10] Z. Gao, Z. Zhou, M. S. Qian, and J. Lin, "Active fault tolerant control scheme for satellite attitude system subject to actuator time-varying faults," *IET Control Theory Appl.*, vol. 12, no. 3, pp. 405–412, Feb. 2018.

[11] Z. Wang, J. Zhou, J. Wang, W. Du, J. Wang, X. Han, and G. He, "A novel fault diagnosis method of gearbox based on maximum kurtosis spectral entropy deconvolution," *IEEE Access*, vol. 7, pp. 29520–29532, 2019.

[12] Y.-X. Shen, Q.-N. He, X.-F. Yang, and Z.-P. Zhao, "Actuator fault reconstruction and fault-tolerant control of wind energy conversion system," *Control Theory Appl.*, vol. 32, pp. 413–420, Mar. 2015.

[13] Z. Wang, G. He, W. Du, J. Zhou, X. Han, J. Wang, H. He, X. Guo, J. Wang, and Y. Kou, "Application of parameter optimized variational mode decomposition method in fault diagnosis of gearbox," *IEEE Access*, vol. 7, pp. 44871–44882, 2019.

[14] M. E. N. Sørensen, S. Hansen, M. Breivik, and M. Blanke, "Performance comparison of controllers with fault-dependent control allocation for UAVs," *J. Intell. Robotic Syst.*, vol. 87, pp. 187–207, Jul. 2017.

[15] C. Zhang, J. Wang, D. Zhang, and X. Shao, "Fault-tolerant adaptive finite-time attitude synchronization and tracking control for multi-spacecraft formation," *Aerosp. Sci. Technol.*, vol. 73, pp. 197–209, Feb. 2018.

[16] A. Shamisa and Z. Kiani, "Robust fault-tolerant controller design for aerodynamic load simulator," *Aerosp. Sci. Technol.*, vol. 78, pp. 232–341, Jul. 2018.

[17] A. Abbaspour, P. Aboutalebi, K. K. Yen, and A. Sargolzaei, "Neural adaptive observer-based sensor and actuator fault detection in nonlinear systems: Application in UAV," *ISA Trans.*, vol. 67, pp. 317–329, Mar. 2017.

[18] Y. M. Zhang, A. Chamseddine, C. A. Rabbath, B. W. Gordon, C.-Y. Su, S. Rakheja, C. Fulford, J. Apkarian, and P. Gosselin, "Development of advanced FDD and FTC techniques with application to an unmanned quadrotor helicopter testbed," *J. Franklin Inst.*, vol. 350, no. 9, pp. 2396–2422, Nov. 2013.

[19] J. Zhang, X. Zhao, F. Zhu, and H. Karimi, "Reduced-order observer design for switched descriptor systems with unknown inputs," *IEEE Trans. Autom. Control*, to be published. doi: 10.1109/TAC.2019.2913050.

[20] Z. Wang, L. Zheng, W. Du, W. Cai, J. Zhou, J. Wang, X. Han, and G. He, "A novel method for intelligent fault diagnosis of bearing based on capsule neural network," *Complexity*, vol. 2019, Jun. 2019, Art. no. 6943234.

[21] Z. Wang, W. Du, J. Wang, J. Zhou, X. Han, Z. Zhang, and L. Huang, "Research and application of improved adaptive MOMEDA fault diagnosis method," *Measurement*, vol. 140, pp. 63–75, Jul. 2019.

[22] J. I. Giribet, C. D. Pose, A. S. Ghersin, and I. Mas, "Experimental validation of a fault tolerant hexacopter with tilted rotors," *Int. J. Elect. Electron. Eng. Telecommun.*, vol. 7, no. 2, pp. 58–65, Jan. 2018.

[23] Z. Wang, J. Wang, W. Cai, J. Zhou, W. Du, J. Wang, G. He, and H. He, "Application of an improved ensemble local mean decomposition method for gearbox composite fault diagnosis," *Complexity*, vol. 2019, May 2019, Art. no. 1564243. doi: 10.1155/2019/1564243.

[24] Z. Yu, Y. Qu, and Y. Zhang, "Fault-tolerant containment control of multiple unmanned aerial vehicles based on distributed sliding-mode observer," *J. Intell. Robotic Syst.*, vol. 93, pp. 163–177, Feb. 2019.

[25] B. Wang and Y. Zhang, "Adaptive sliding mode fault-tolerant control for an unmanned aerial vehicle," *Unmanned Syst.*, vol. 5, no. 4, pp. 209–221, Oct. 2017.

[26] P. Li, X. Yu, X. Peng, Z. Zheng, and Y. ZhangEmail author, "Fault-tolerant cooperative control for multiple UAVs based on sliding mode techniques," *Sci. China Inf. Sci.*, vol. 60, May 2017, Art. no. 070204.

[27] N. Djeghali, S. Djennoune, M. Bettayeb, M. Ghanes, and J.-P. Barbot, "Observation and sliding mode observer for nonlinear fractional-order system with unknown input," *ISA Trans.*, vol. 63, pp. 1–10, Jul. 2016.

[28] C. P. Tan and C. Edwards, "Sliding mode observers for robust detection and reconstruction of actuator and sensor faults," *Int. J. Robust Nonlinear Control*, vol. 13, pp. 443–463, Apr. 2003.

[29] J. Zhang, F. Zhu, H. R. Karimi, and F. Wang, "Observer-based sliding mode control for T-S fuzzy descriptor systems with time-delay," *IEEE Trans. Fuzzy Syst.*, to be published. doi: 10.1109/TFUZZ.2019.2893220.
[30] C. L. Li, X. Q. Chen, Q. X. Jia, and Y. H. Geng, "FDD of the attitude control system of satellite with actuator fault and time delay via two-stage kalman filter," *Appl. Mech. Mater.*, vol. 441, pp. 859–863, Dec. 2013.
[31] Z. Cen, H. Noura, B. T. Susilo, and Y. A. Younes, "Robust fault diagnosis for quadrotor UAVs using adaptive thau observer," *J. Intell. Robotic Syst.*, vol. 73, nos. 1–4, pp. 573–588, Jan. 2014.
[32] A.-R. Merheb, H. Noura, and F. Bateman, "Design of passive fault-tolerant controllers of a quadrotor based on sliding mode theory," *Int. J. Appl. Math. Comput. Sci.*, vol. 25, no. 3, pp. 561–576, Sep. 2015.
[33] B. Wang and Y. Zhang, "An adaptive fault-tolerant sliding mode control allocation scheme for multirotor helicopter subject to simultaneous actuator faults," *IEEE Trans. Ind. Electron.*, vol. 65, no. 5, pp. 4227–4236, May 2018.
[34] J. I. Giribet, R. S. Sanchez-Pena, and A. S. Ghersin, "Analysis and design of a tilted rotor hexacopter for fault tolerance," *IEEE Trans. Aerosp. Electron. Syst.*, vol. 52, no. 4, pp. 1555–1567, Aug. 2016.
[35] S. Zeghlache, A. Djerioui, L. Benyettou, T. Benslimane, H. Mekki, and A. Bouguerra, "Fault tolerant control for modified quadrotor via adaptive type-2 fuzzy backstepping subject to actuator faults," *ISA Trans.*, to be published. doi: 10.1016/j.isatra.2019.04.034.
[36] X. Gong, Y. Bai, and C. J. Zhao, "Hex-Rotor aircraft and its autonomous flight control system," *Opt. Precis. Eng.*, vol. 20, no. 11, pp. 2450–2458, Nov. 2012.
[37] C. J. Zhao, "Fault analysis of execution units and flight control for hex-rotor unmanned aerial vehicle," Ph.D. dissertation, Dept. CIOMP, Univ. Chin. Acad. Sci., Beijing, China, 2015.
[38] M. Elzoghby, U. Arif, F. Li, and Z. Yu, "Investigation of adaptive robust Kalman filtering algorithms for GPS/DR navigation system filters," in *Proc. IOP Conf. Ser., Mater. Sci. Eng.*, Hong kong, Mar. 2017, Art. no. 012019.
[39] M. Y. Fu, Z. H. Deng, and J. W. Zhang, *Kalman Filtering Theory and its Application in Navigation System*, 2nd ed. Beijing, China: Sci. Press, 2010, pp. 108–118.

RIJUN WANG received the Ph.D. degree from the Changchun Institute of Optics, Fine Mechanics and Physics, Chinese Academy of Sciences, Changchun, China. He is currently a Lecturer with the North University of China. His research interests include the fault diagnosis of unmanned aerial vehicles and fault tolerant control.

CHANGJUN ZHAO received the Ph.D. degree from the University of Chinese Academy of Sciences, Beijing, China. He is currently a Senior Engineer with the China Electronic Product Reliability and Environmental Testing Research Institute. His research interests include the modeling and the control of complex systems, and nonlinear system control.

YUE BAI received the Ph.D. degree from the Changchun Institute of Optics, Fine Mechanics and Physics, Chinese Academy of Sciences, Changchun, China, where he is currently a Researcher. He was a Visiting Scholar with Manchester University, from 2008 to 2010. His research interests include unmanned system dynamics, modeling, and control.

WENHUA DU received the Ph.D. degree from Tianjin University, Tianjin, China. She was a Visiting Scholar with Warwick University, from 2016 to 2017. She is currently a Professor with the North University of China. Her research interests include mechanical dynamics and machine vision.

JUNYUAN WANG received the Ph.D. degree from the Taiyuan University of Technology, in 2008. He is currently a Professor with the North University of China, the Vice Chairman of the Shanxi Province Society of Vibration Engineering, and the Executive Director and the Deputy Secretary-General of the Shanxi Province Mechanical Engineering Society, where he is also the Vice Chairman of the Mechanical Transmission Branch. His research interests include intelligent manufacturing technology and systems.